Applied Surface Science 569 (2021) 150909

Contents lists available at ScienceDirect

Applied Surface Science

journal homepage: www.elsevier.com/locate/apsusc

Full Length Article

Photoluminescence imaging of defects in TiO_2: The influence of grain boundaries and doping on charge carrier dynamics

Dominik Wrana [a,*], Thomas Gensch [b], Benedykt R. Jany [a], Karol Cieślik [a], Christian Rodenbücher [c], Grzegorz Cempura [d], Adam Kruk [d], Franciszek Krok [a]

[a] Marian Smoluchowski Institute of Physics, Jagiellonian University, Krakow, Poland
[b] Institute of Biological Information Processing (IBI-1), Forschungszentrum Jülich, Jülich, Germany
[c] Institute of Energy and Climate Research (IEK-14), Forschungszentrum Jülich, Jülich, Germany
[d] International Centre of Electron Microscopy for Materials Science, Faculty of Metals Engineering and Industrial Computer Science, AGH University of Science and Technology, Krakow, Poland

ARTICLE INFO

Keywords:
Photoluminescence
TiO_2
Dislocations
Boundary
Charge carrier lifetimes
Photocatalysis

ABSTRACT

Understanding the mechanisms of charge generation and their recombination in rutile TiO_2 is of key importance in the design of optoelectronic and photocatalytic devices. In this study, we investigate the impact of both extrinsic and intrinsic defects on photoluminescence (PL) decay dynamics. The exploitation of two-photon fluorescence lifetime imaging microscopy (FLIM) enabled differentiation to be made between photoluminescence originating from dislocations and bulk in Nb-doped rutile TiO_2. It was found that dislocations pinned at grain boundaries feature lower photoluminescence intensity and faster decay times (by 100 ps) than those in the bulk. This can be reversed upon reduction, whereby trap states are preferentially formed near to dislocation sites. We also evaluated the dependence of the extrinsic doping level on the charge carrier dynamics of rutile, and show that PL lifetimes are governed by predominant Auger processes that are insensitive to reduction, unlike dislocations. We believe that the oxygen deficiency suppression of charge carrier recombination at grain boundaries is the key factor in improving the photocatalytic activity of real TiO_2-based materials.

1. Introduction

Titanium oxides present themselves as promising materials with respect to various (photo)catalytic applications, mostly because of the ease of bandgap engineering via reduction, which is currently being widely investigated [1-3]. Many research groups have studied the key limiting factors against achieving high efficiencies, namely charge carrier dynamics, separation and recombination processes in both anatase and rutile TiO_2 [4-7], whereas the (1 1 0) surface of the latter offers good electron extraction performance in perovskite-TiO_2 solar cells [8]. Most promising materials are characterized by the purposely-induced high density of defects, especially oxygen vacancies, e.g., oxygen-deficient TiO_2 is a promising candidate for photoelectrochemical water-splitting [9] and energy storage applications [10]. However, it has been reported that even though so-called black TiO_2 offers a narrow bandgap, and therefore a great absorption range [11], it possesses downsides such as the high density of bulk vacancy defects acting as recombination sites and reducing the photocatalytic activity [12]. On the other hand, supplying the crystal with one-dimensional defects such as edge dislocations can both narrow the bandgap of TiO_2 [13] and provide trap centers for electrons [14]. It was recently experimentally-demonstrated that dislocations help considerably enhance photocatalytic activities owing to the modification of bandgaps by applying strain [2,15]. The use of oxygen-deficient high grain boundary density TiO_2 anodes for sodium-ion batteries has been shown to greatly enhance both the performance and stability of energy storage devices [16]. The same idea lies behind the improvement of lithium-oxygen battery performance on the basis of using high-grain boundary nanoporous TiO_2 as an electrocatalyst [17]. Importantly, dislocations can be mechanically-induced in transition metal oxides, which allows for the tailoring materials with desired properties [18].

This relationship between the properties of oxides and the presence of defects of different dimensionalities is not always fully understood, and therefore a model system with precisely controlled density defects is needed. One such extensively-investigated system is bicrystal, whereby one can analyze not only the influence of point defects but also extended

* Corresponding author.
E-mail address: dominik.wrana@uj.edu.pl (D. Wrana).

https://doi.org/10.1016/j.apsusc.2021.150909
Received 23 February 2021; Received in revised form 16 July 2021; Accepted 7 August 2021
Available online 10 August 2021

defects, which are of key importance in real materials [19]. Bicrystal boundaries are sites that contain a multitude of dislocations, wherein the type and spacing can be controlled by changing the tilt angle [20,21]. The broken symmetry results in strain gradients that give rise to the remarkable electrical and mechanical properties of dislocations [22]. Dislocations in oxide materials have been the subject of simulations that show that they can be a site of preferential reduction and increased diffusion [23 24]. All of the abovementioned factors make bicrystal boundaries fascinating model systems for understanding the properties of real polycrystalline or ceramic materials. Bicrystals are typically artificially-synthesized by cutting two crystals, polishing their surfaces, joining them at the desired angle and, finally, heating them in the air at elevated temperatures and high pressures for many hours (e.g., 10 h at 1500 °C for TiO_2 [25]). However, it has been shown through the analysis of etched surface patterns that bicrystal production process induces the formation of new dislocations, even far from the boundary [25,26] and therefore synthetic bicrystals do not fully reflect the boundary's natural state. In this study, we investigate a bicrystal that has naturally formed during typical crystal synthesis and which has not been additionally pressed or annealed, and which therefore most faithfully reflects the ideal grain boundary as a line of dislocations.

Herein, we determine the impact of dislocations present at the low-angle boundary on the key factor limiting photocatalytic activity, namely the dynamics of photogenerated charge carriers. Although a few recent papers focused on the electro- and cathodoluminescence intensities of differently formed dislocations and boundaries [27-29], a more detailed information of the temporal behavior of charge carriers is needed. The intensity of photoluminescence (PL) is used as a measure of the recombination of the generated excitations [30], whereas the decay profiles shed light on the mechanisms of photocatalysis [31]. It is the idea of designing active layers with longer carrier lifetimes driving the development of highly-efficient tandem solar cells [32]. However, traditional PL measurements do not provide spatially-resolved data – in order to obtain such information at the microscale, it is necessary to utilize fluorescence lifetime imaging microscopy (FLIM). FLIM is a technique that enables photoluminescence imaging in a time domain and is widely used in the life sciences [33,34], but also finds applications in areas ranging from investigations of recombination in the grain boundaries of solar cells [35] to the identification of paint pigments and the study of their decay in time period dating in the conservation sciences [36-40]. We employ two-photon FLIM microscopy equipped with time-correlated single-photon counting in order to achieve the best temporal sensitivity and spatial resolution below a single micrometer. This enabled, for the first time in the case of titanium oxides, the separation of signals from the bulk, dislocations, and area close to the grain boundary. By using a low concentration of pentavalent niobium dopant in rutile TiO_2 crystals with a low-angle bicrystal boundary and annealing them under oxidizing or reducing conditions, we address the question of what the impact is of extrinsic and intrinsic defects on the photoluminescence process and, therefore, on the recombination efficiency. In this paper, we prove that two-photon excitation photoluminescence microscopy enables differentiation to be drawn between the charge carrier dynamics in bulk and dislocations, as well as the effects of oxygen vacancy self-doping upon reduction and aliovalent Nb doping.

2. Materials and methods

In order to investigate the photoluminescent properties originating from defect states, we selected bulk rutile TiO_2 crystals. We used Verneuil-grown undoped and Nb-doped TiO_2(110) epi-polished rutile single crystals (Shinkosha Co. Ltd.) with dimensions of 10 × 3 × 0.5 mm^3. Two nominal Nb doping levels were utilized: 0.5 wt% (0.43 at.%) (for most experiments) and 1 wt% (0.86 at.%). In the case of 0.5% Nb-doped TiO_2(110), the presence of a natural bicrystal boundary was detected, which featured a tilt angle of ~ 1°. Samples containing a bicrystal boundary were either oxidized (1 h, 1000 °C, 200 mbar O_2) or reduced (1 h, 1000 °C, vacuum pressure of 10^{-6} mbar) in a high-vacuum (HV) quartz tube heated in a furnace. Bicrystals were investigated using an FEI Quanta 3D FEG field-emission scanning electron microscope (SEM), where the electron backscatter diffraction (EBSD) method was utilized for determining tilt angles. For the transmission electron microscopy (TEM) measurements, a thin lamella was cut across the grain boundary using a gallium focused ion gun. The chemical mapping of Nb, O and Ti (by means of energy-dispersive X-ray spectroscopy, EDX) and nano-beam diffraction (NBD) measurements were carried out in a Titan Cubed G2 60–300 microscope, equipped with an X-FEG Schottky high-brightness source and a monochromator. Strain field maps were calculated with the geometric phase analysis (GPA) [41] of atomically-resolved HAADF STEM images using the Strain++ software [42].

The FLIM measurements determining the spatial distribution of photoluminescence lifetimes were performed at room temperature using an upright scanning fluorescence microscope (A1R; Nikon) equipped with a water immersion objective (NA 1.1) with a pulsed high-repetition rate Ti:Sa-laser (λ_{exc} = 740 nm (1.68 eV); 100 fs pulse width; 80 MHz repetition rate; MaTai HP DeepSee; Spectra Physics, Newport Cooperation, Santa Clara, CA, USA) for two-photon excitation. The incident laser intensity amounted to ca. 1.4 × 10^{17} photons/pulse cm^{-2}. The images were generated by a raster scanning (512 × 512 pixels) focused laser beam over the sample with a minimum estimated voxel size of approximately 1.5 μm in z (i.e., perpendicular to the sample surface) and 0.82 μm in the lateral, x and y directions. The time course of the photoluminescence intensity (decays) passing a broadband emission filter (410–650 nm) was detected by a GaAsP-hybrid photodetector (HPM-100–40, Becker & Hickl, Berlin, Germany) operating in single-photon counting mode and reconstructed and analyzed for each pixel by means of time-correlated single-photon counting (TCSPC) electronics (Simple-Tau, Becker & Hickl) and software (SPCM64 and SPCImage 8.0, Becker & Hickl). Photoluminescence decays at each pixel were fitted by a single exponential function, yielding a reasonable χ^2 parameter below 2 for each pixel (mostly in the range of 0.8–1.5). Only the PL decays from undoped TiO_2(110) crystals were fitted by a bi-exponential function and the slower decay times were compared.

3. Results and discussion

3.1. Structure and composition

SEM and TEM investigations were performed in order to determine the structure and composition of the low-angle bicrystal boundaries in Nb-doped (0.5% wt.) rutile TiO_2 crystals. An EBSD texture analysis confirmed an angle of one degree separating two single crystals (Fig. 1 a–c). Both crystals had an exposed (110) surface, which is the most thermodynamically-stable. Up until now, the majority of TiO_2 bicrystals analyzed had larger tilt boundary angles of between 5 [14] and 66° [43]. Such a small angle as that used in the presented case limits the interaction between neighboring dislocations in a boundary, making results easier to generalize. To directly verify the dislocation structure and crystallinity, a lamella across the bicrystal boundary was cut from a region marked in green in Fig. 1a. The HAADF-STEM image reveals a periodic contrast at the boundary, as shown in Fig. 1d, suggesting an array of individual dislocations separated by 36 nm, propagating in the (010) direction. The monocrystalline rutile structure was found in both crystals, as demonstrated by a selected-area electron diffraction (SAED) pattern (Fig. 1d insets). There was no evidence of secondary phase formation near this grain boundary.

Although the structural impact of the dislocations present at the boundary is limited to their nearest vicinities, there could be a compositional effect from reaching out further. To address this issue, detailed EDX data were collected (Fig. 2). No significant difference was observed in the concentration of the three elements (Nb, Ti, O) between the dislocation cores and the pure bulk crystal, as can be seen in the maps (Fig. 2 a) and on the integrated spectra (Fig. 2 b–e). This was also shown

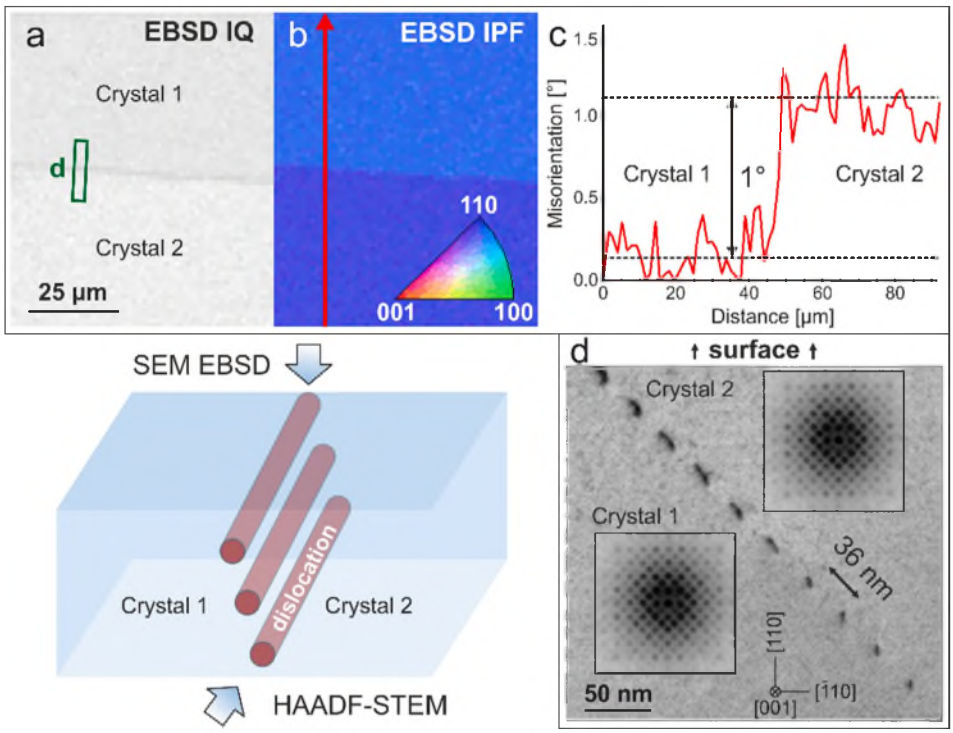

Fig. 1. Natural TiO_2:Nb (1 1 0) boundary structure. (a), (b), (c) Electron backscatter diffraction (EBSD) image quality and inverse pole figure (IPF) maps, providing ~ 1-degree tilt-angle between the two crystals. (d) HAADF-STEM image of the boundary, showing an array of dislocations (dark spots); insets: SAED patterns depicting [0 0 1] zone axis diffraction of rutile TiO_2.

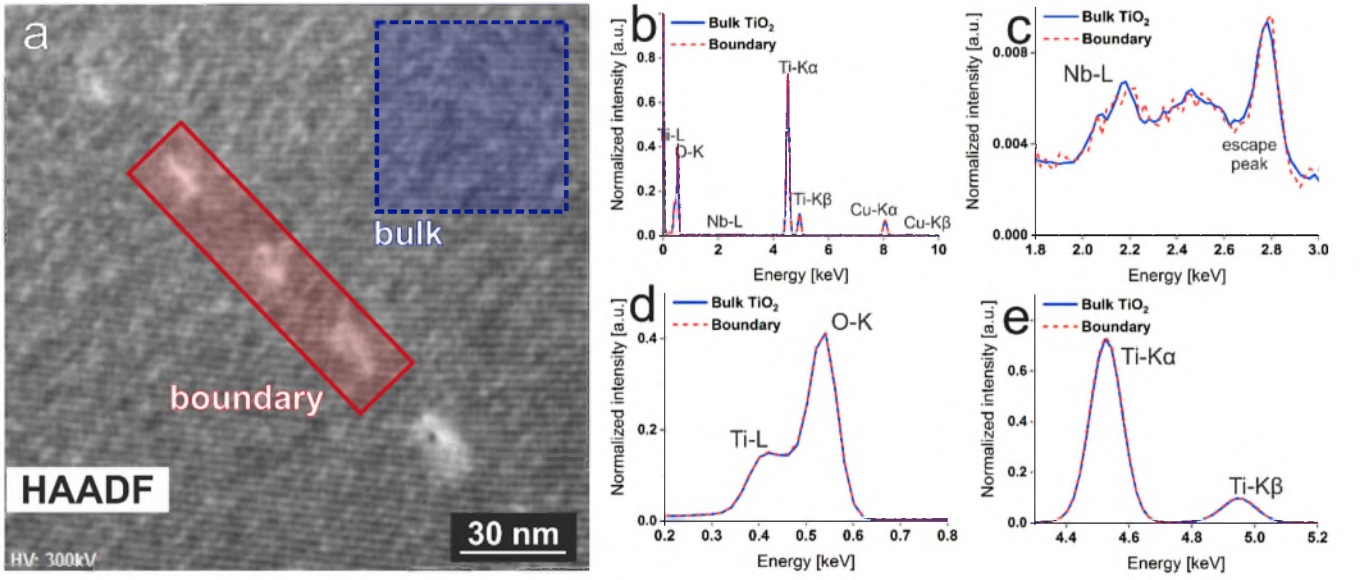

Fig. 2. Chemical composition at the TiO_2:Nb boundary. (a) HAADF-STEM image of the investigated region. (b) EDX spectrum overview and particular spectra exhibiting no significant difference in (c) Nb-L, (d, e) Ti-L, Ti-K and O-K lines from TEM EDX.

by the SEM EDX in the boundary area (see Fig. S2 in the Supplementary). Comparing the EDX spectra near the Nb-L line energy between the dislocation core and pure bulk region, one can conclude that if there is a relative difference in niobium concentrations between the two regions, it should be smaller than ~ 11% (at the level of one standard deviation) from the statistical signal to background considerations, comparing the variance of counts at the Nb-L peak across the dislocation to the mean value. Such a lack of Nb signal enhancement at the grain boundary appears to not be the general case for all transition metal oxides, e.g., Nb-doped $SrTiO_3$ [44]. Literature studies on TiO_2 ceramics prove that segregation occurs in Ce-doped samples; however, in the Nb-doped samples, dopant segregation is limited [45]. Cathodoluminescence experiments performed on $SrTiO_3$ crystals suggest enhanced oxygen migration at dislocations [27], but the oxygen concentration appears to be unchanged in the case of TiO_2, as depicted in Fig. 2b and d.

A closer look at the atomic arrangement in the individual dislocations is provided in Fig. 3a by the HAADF-STEM. A pair of edge-on dislocations is located at each spot, with the missing half-planes in the (1 1 0) and (−1 1 0) directions. The rutile crystal appears to be defect-free in-between the dislocations. In order to visualize the strain

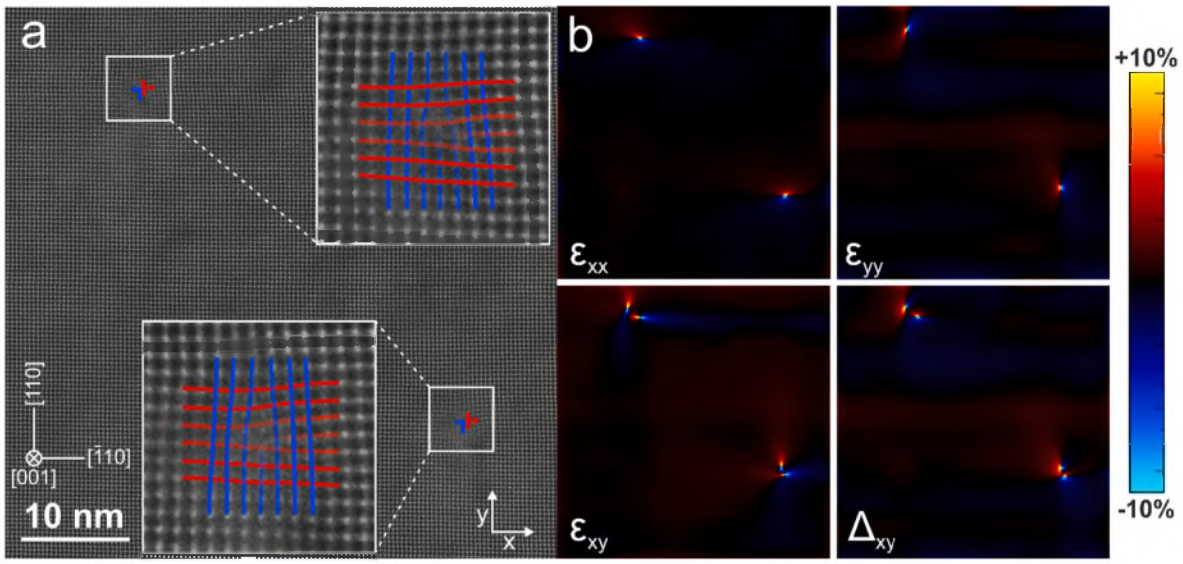

Fig. 3. Characterization of the structure of the individual dislocations present at the boundary. (a) Atomic-resolution HAADF-STEM image of a boundary viewed from the [001] projection. (b) GPA analysis strain maps (ε_{xx}, ε_{yy}, ε_{xy}, Δ_{xy}) at the boundary.

gradients emerging from dislocations, geometric phase analysis (GPA) was employed, providing strain matrix elements (ε_{xx}, ε_{yy}, ε_{xy}) and dilatation (Δ_{xy}), which is a trace of the distortion matrix. The calculated values of those coefficients shown in Fig. 3b indicate lattice distortions of up to 10% in the nearest vicinity of the dislocation, stretching out up to 5 nm from the core, with no significant distortions thereafter. Such strain fields originating from the dislocations affect the electronic structure of the surrounding crystal, which can in turn lead to an enhancement in photocatalytic activities by decreasing the band gap and supplying greater density to the states in their vicinity [15]. Band-bending limits the motion of the charge carriers, which makes both electrons and holes more likely to separate and localize, enhancing the photocatalytic activity of TiO_2 [46]. However, the opposite effect of enhanced electron mobility along dislocations, which makes them conducting channels in the TiO_2 matrix [13,47,48,49] should decrease the likelihood of electron localization near the dislocations. Dislocations in rutile TiO_2 are expected to provide n-type conduction paths, with overall conductivity depending on the overlap of space charge zones [49] In order to resolve which mechanism is predominant in the rutile TiO_2, it is necessary to directly measure the lifetime of charge carriers at the boundary.

3.2. *Photoluminescence*

Having demonstrated that the bicrystal boundary consists of an array of equidistantly-spaced dislocations and no significant difference in the chemical composition is observed, we will now address the impact of dislocations on optoelectronic properties as measured by means of two-photon FLIM. Although many studies have attempted to correlate PL intensity with the photocatalytic activity of titanium oxides [50,51], it is commonly accepted that the PL lifetime is a significantly better measure of the PL, as the emission intensity is strongly dependent on many factors, which include crystal structure, particle size, and optical configuration [39]. We employed a high-power pulsed laser with photon energy (1.68 eV) that was smaller than the bandgap (3.1 eV) to excite the crystal via two-photon absorption and detect both the PL intensity and lifetime of the sample. Two-photon absorption is a non-linear process that depends on the illumination power squared, and therefore the spatial resolution is enhanced by comparison to one-photon absorption, amounting in our microscope to about 300 nm laterally and 500 nm out-of-plane (see Fig. 4i). This makes the two-photon PL mapping a tool of choice for the characterization of grain boundaries, capable of identifying even individual dislocation bunches, as we demonstrated recently in the case of an $SrTiO_3$ bicrystal [26]. Two-photon PL measurements can also help overcome one of the biggest factors limiting progress in understanding the performance of real thin film-based devices, namely the inability to identify grain boundaries using other methods than electron microscopy [52]. Additionally, two-photon FLIM measurements of photoluminescence allow for the much faster investigation of large sample areas (100 s of μm^2 in one minute) and do not entail a demanding sample-preparation method.

In the case of simple undoped rutile TiO_2, PL decay has a double exponential character with two distinguishable deactivation channels: slow and fast. The slow decay channel characterized by a longer photoluminescence decay time is commonly attributed to the recombination of excitons via oxygen defects [53]. Such defects, present on either the surface or in bulk, serve as trap centers for electrons, suppressing the carrier recombination [54]. Additionally, trapped electrons on oxygen vacancies scatter free electrons, decreasing their mobility, which thereby helps to separate electron-hole pairs and finally increases their lifetime [53]. The fast PL decay component is likely associated with direct electron hole recombination in the bulk [55]. The situation for the Nb donor-doped rutile investigated here is straightforward, and is characterized by a single exponent, leaving only slow decay. For each sample, one exponential fit with one parameter set for the PL temporal behavior was obtained. Single decay characteristics for both bulk TiO_2 and the bicrystal boundary are shown in Fig. 4g and h. The TiO_2 PL lifetimes obtained from the batch-fitting of decay characteristics at each pixel are plotted in Fig. 4a–c and the corresponding intensities are shown in Fig. 4d–f.

In rutile TiO_2, titanium atoms present at the dislocation cores have a mixed 3+/4 + valence that is based on calculations that suggest the confinement of those states [13]. Therefore, the boundary area, which is enriched in dislocations, should behave differently when exposed to light. This is visually depicted in Fig. 4b and e, where the bicrystal boundary, being in principle an arranged line of dislocations, has a shorter PL lifetime and lower intensity than the TiO_2 matrix, which is homogeneous. Literature studies suggest dislocations in TiO_2 acting as traps for electrons but not holes, making recombination less effective [14]. This was directly proven by our PL measurements, which showed less intensity of PL at the boundary compared to the bulk TiO_2 (Fig. 4e). Such behavior is also reflected in the PL lifetimes shown in Fig. 4b: for the stoichiometric sample (s-TiO_2), the PL lifetime at the boundary is 200 ps lower than in the bulk. Moreover, a region around the boundary a

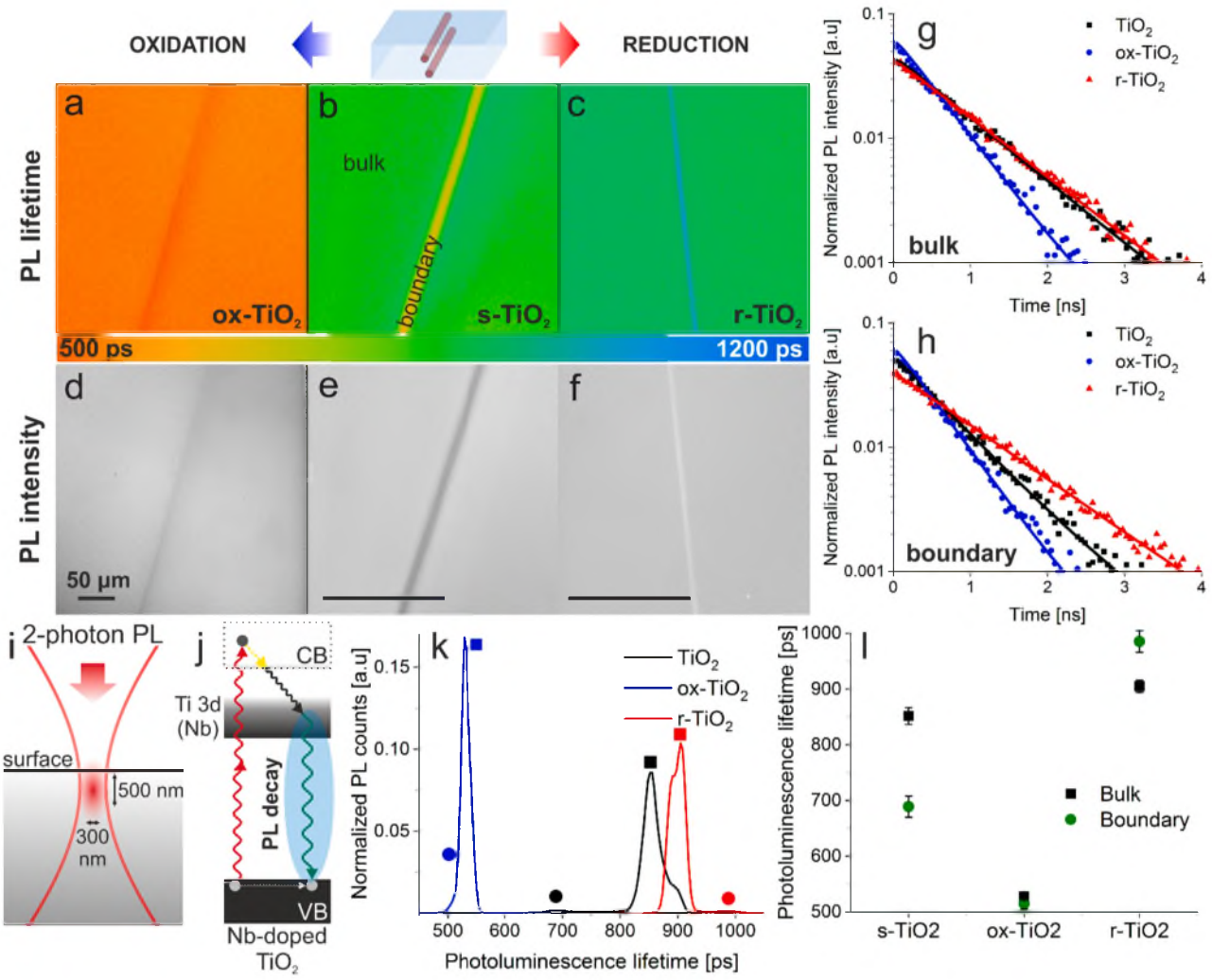

Fig. 4. Photoluminescence (PL) lifetime and intensity maps of the (a, d) oxidized (ox-TiO_2:Nb), (b, e) stoichiometric (s-TiO_2:Nb), and (c, f) reduced (r-TiO_2:Nb) bicrystal boundary. All of the lifetime maps feature a common linear color scale (500–1200 ps). The black bars indicate a 50 μm lateral scale. (g, h) PL decay profiles for the bulk and boundary, respectively. (i, j) Two-photon excitation PL microscopy scheme and a simple model of PL generation in Nb-doped TiO_2. (k) PL lifetime distributions for stoichiometric, reduced, and oxidized samples with bulk (■) and boundary (●) indicated for each sample. (l) Summarized average PL lifetimes for each sample and area.

few micrometers-wide features slightly higher PL lifetimes (ca. 50 ps) than the boundary itself, which is visible as a shoulder in the PL lifetime histograms shown in Fig. 4k. This could be understood as either a consequence of induced ionic polarization in the crystal or as a result of a space charge zone similar to that observed in $SrTiO_3$ [56,57] and the TiO_2 bicrystal boundaries [58]. It is worth noting that the substantial impact observed on PL intensity and dynamics at the boundary is a result of light interaction with a line of sparsely-distributed dislocations, with a separation of 36 nm (Fig. 1). For grain boundaries in real polycrystalline films, the influence would be more significant, as the dislocation density there is much higher.

The PL mechanism induced by two-photon absorption is depicted in Fig. 4j. With a sufficiently high density of incident photons, as illuminated by the pulsed laser excitation, an electron-hole pair is created by two quasi-simultaneous absorption events of photons with the energy lower than the bandgap, which was 1.68 eV in this case. The electron was excited to the conduction band with an energy of 3.36 eV above the valence band maximum. Then, it returned to the lowest available allowed state and relaxed from there to the ground state in accordance with Kasha's rule, emitting a PL photon with a high probability (quantum yield). In rutile TiO_2(1 1 0), 0.5% Nb extrinsic doping induces a state 0.8 eV below the conduction band minimum [59]. It is mostly the Ti 3d state, which originates from oxygen vacancies [1,60], with a small contribution from Nb 4d [59]. The excess electron in the doped rutile is mainly localized at the adjacent Ti atoms and partially at the Nb site itself, and is much more localized than in the Nb-doped anatase TiO_2 [59]. As we measure PL dynamics at room temperature, such a state is considered a deep-level trap. From this state, a radiative recombination occurs that results in a green PL emission, measured here both in terms of intensity and, more importantly, lifetime. The emission maximum of Nb-doped TiO_2 is located at around 440 nm [39], with a broad tail of up to 650 nm [61]. The reason would be similar to the case of undoped TiO_2, where bandgap states as well as self-trapped exciton states exhibit a wide range of configurations that explain the broad emission spectral width [62].

The situation at the grain boundary is different, as the crystallographic order is disrupted and so is the electronic structure. For the undoped rutile TiO_2, the dislocation core region is associated with a band of unoccupied states extending 0.3 eV below the bulk conduction band minimum, with no corresponding occupied states above the valence band maximum [14]. This suggests that a dislocation would serve as a 1D trap for electrons but not holes, as was also observed for dislocations in MgO [63]. However, in the case of the substitutional doping of Nb in TiO_2, these states most likely lie above doping-induced

Ti 3d levels and the trapping mechanism is suppressed, as it is energetically less favourable. This was proven by PL measurements (Fig. 4), when a decrease in the PL lifetime at the boundary is observed. The higher mobility of charge carriers along dislocations [13,47] increases the cross-section for non-radiative Auger processes, in turn decreasing the PL lifetimes. This appears to be a more general situation, as lower PL lifetimes at the grain boundaries were also measured for the case of the as-grown multicrystalline Si [64].

Having described the role of extended defects in the grain boundaries on PL dynamics, it is now necessary to address the influence of point defects in TiO_2, especially oxygen vacancies, whose concentration governs most electronic and structural properties.

The thermal reduction of rutile TiO_2 results in self-doping by oxygen vacancies [65], whereas for Nb-doped crystals, an additional Nb segregation occurs [3,66]. For the mild reduction conditions (1000 °C, UHV), an out-of-plane depletion of niobium is observed to the depth of tens of nanometers, simultaneously forming an Nb-rich conductive layer with a new reconstruction on the (1 1 0) surface [3]. As the FLIM signal is averaged almost a micrometer in the axial direction, this resegregation does not affect the PL decay due to its very low relative contribution to the total signal. Here, the ordered array of dislocations at the boundary is preserved and no structural changes were noted (see Figure S3 in the Supplementary Material). Although the reduction does not change the PL dynamics in the bulk, the situation at the boundary is different. For a stoichiometric crystal, the boundary has a slower and less intense PL; however, when the crystal is reduced, this situation is reversed (Fig. 4c, f). Bulk PL decay does not change after reduction, whereas the PL lifetime of a boundary increases substantially, by 300 ps (compare Fig. 4l). This suggests that electrons are more efficiently trapped at reduced dislocation sites, as levels lie deeper in the gap and are close to the valence band maximum [14]. In transition metal oxides, dislocations and therefore grain boundaries are more efficiently reduced than the matrix [19,26,67-69] and produced oxygen vacancies serve as effective trap states, helping to separate and localize photogenerated charge carriers. Recent studies conducted on the Nb-doped $SrTiO_3$ films prove that increased electroluminescence at the formed conducting paths are related to the increased amount of defect states associated with oxygen vacancies[28]. [67]This could be the reason for the strong correlation observed between photo-induced exciton pair lifetimes and the photocatalytic activity of nanocrystalline titania [51]. Other studies suggest that Ti^{3+} states induced by edge dislocations improve photocatalytic activity by up to two times compared to dislocation-free TiO_2 nanowires [2]; however, according to our results, these are most likely reduced dislocations.

Oxidation significantly decreases the PL lifetimes for both TiO_2 bulk and grain boundary (see Fig. 4a, d and Fig. S1 in the Supplementary Material for a comparison of the same area before and after oxidation). This is most likely a result of the induced concentration gradients of Nb. Close to the surface, the concentration of niobium in Nb-doped TiO_2 and annealed under oxidizing conditions is substantially larger than in the bulk phase. At the same time, an increase in titanium vacancies was observed [66]; however, such defects do not influence the lifetimes of photogenerated pairs, as Ti cation vacancies induced by irradiation do not greatly affect positron lifetimes in TiO_2 [70]. The main contribution for decreased PL lifetimes is segregation-induced enrichment in niobium, which results in the formation of an Nb_2TiO_7-type structure [66]. At this point, an increased concentration of pentavalent Nb donates further excess electrons, which, by Auger processes, suppress the radiative recombination of electron-hole pairs, leading to the more rapid relaxation of excited electrons.

The FLIM method provides a possibility for the mapping of charge carrier dynamics at the sub-micrometer scale. Fig. 5 displays a comparison of PL lifetimes at a grain boundary for stoichiometric and reduced Nb-doped TiO_2 crystals. The effective achieved resolution is below 300 nm, based on the FWHM criterion (Fig. 5d). The theoretical

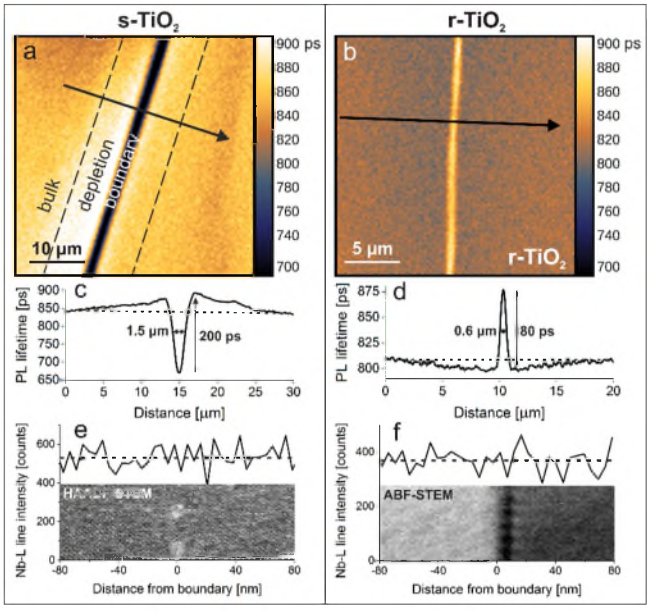

Fig. 5. Spatial information on PL lifetimes and Nb concentrations for stoichiometric (s-TiO_2) and reduced TiO_2 (r-TiO_2). (a) PL lifetime map of stoichiometric TiO_2(1 1 0). (b) PL lifetime of thermally-reduced TiO_2(1 1 0). (c) Line profile taken from (a) across the bicrystal boundary. (d) Line profile taken from (b) across the boundary. (e), (f) EDX Nb-L line intensity profiles across the boundary for stoichiometric and reduced crystals, respectively, exhibiting a uniform Nb concentration for both samples. The insets shows STEM maps for the same areas.

resolution is estimated as $\frac{0.65\lambda}{\sqrt{2}NA^{0.9}}$ for NA > 0.7 [71] and in our case it yields 310 nm (for NA = 1.1 and λ = 740 nm), which means that the FLIM measurements of the boundary have reached their physical limit. However, confined structure of dislocations revealed by TEM suggests that a boundary response originates from the area even smaller, confined to the nearest vicinity of dislocations and presumably the zone of increased amount of oxygen vacancies around, as it was observed for cathodoluminescence measurements of dislocations in $SrTiO_3$ [29]. The bicrystal boundary present in a reduced crystal exhibits a narrower PL response zone to a two-photon excitation (Fig. 5b), which could be also connected to small, in-plane concentration gradients of niobium that emerge during annealing. We consider this effect unlikely, as no significant concentration gradient was measured by EDX TEM. In order to prove this, background-corrected Nb-L line intensity profiles across the boundary are shown in Fig. 5e and f for stoichiometric and reduced crystals, respectively. Although the Nb intensity is low, no systematic differences in the concentration at the boundary are present, proving that the nominal concentration of extrinsic defects is uniform and relative changes are below 11%.

In order to gain insight into the correlation between extrinsic donor concentration and PL dynamics, a set of Nb-doped crystals were measured. Aliovalent doping is known for its beneficial impact on photocatalytic activity, e.g., Fe doping resulted in the enhancement of methylene degradation [72]; however, this dependence on doping concentrations may be non-monotonous, as 0.8 at% Fe-doped TiO_2 films exhibited the highest photocatalytic activity, which then decreased. This was the rationale for us to investigate the impact of the three Nb doping levels (0%, 0.5 wt%, 1.0 wt%) on PL dynamics, the results of which are shown in Fig. 6. There is a clear effect from the increasing of donor doping on PL lifetimes. The undoped rutile TiO_2(1 1 0) crystals feature a long, double-exponential PL decay process, similar to undoped $SrTiO_3$ [26]. The dominating long component, corresponding to oxygen vacancy-mediated recombination [53], has a lifetime of 2 ns, which is significantly increased to 4.6 ns following thermal reduction (Fig. 6a and

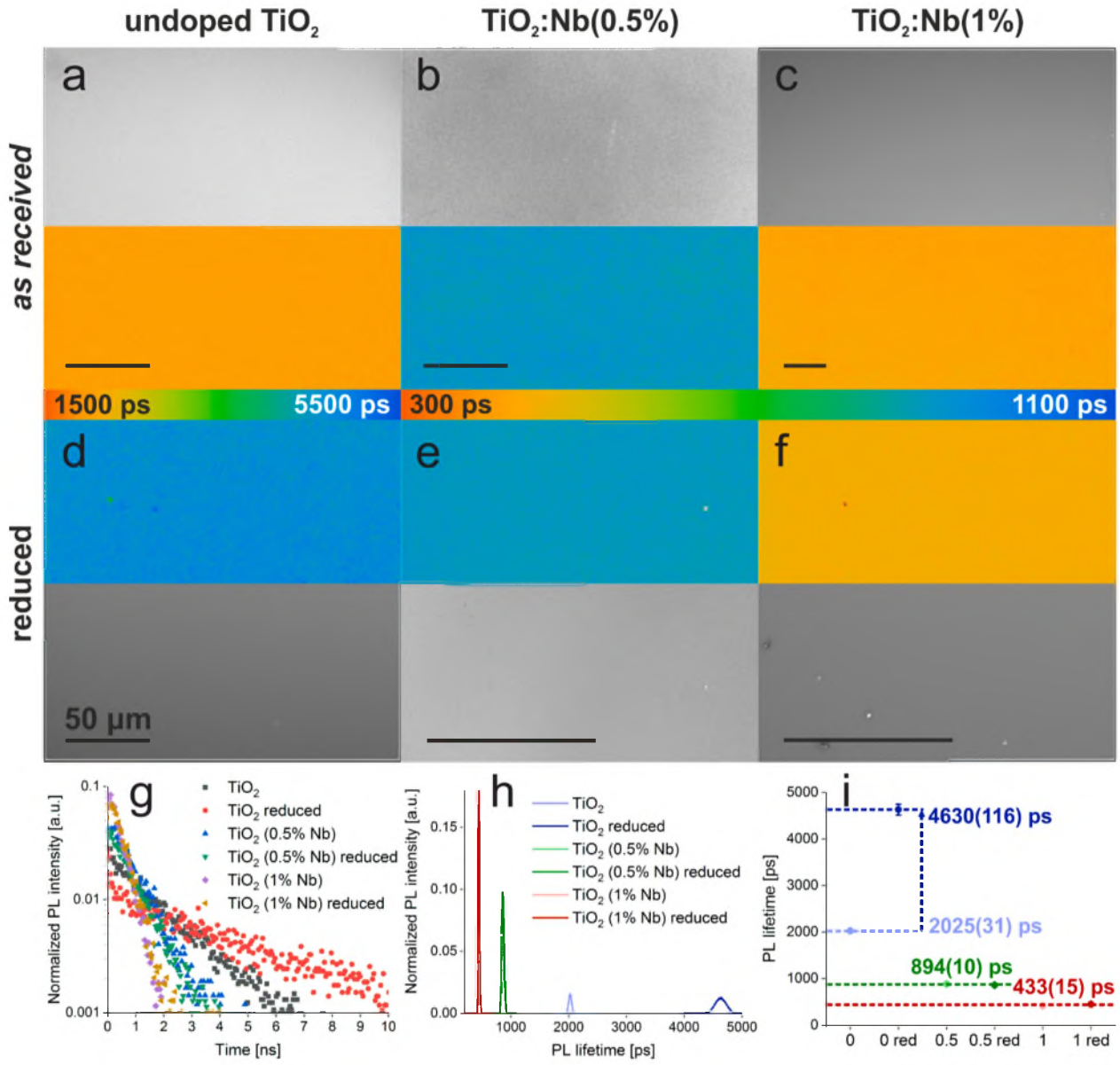

Fig. 6. Nb concentration and reduction influences on PL time-integrated intensities and lifetimes of rutile TiO_2(110). (a, d) undoped TiO_2(110). (b, e) 0.5% Nb doping of TiO_2(110) with a natural bicrystal boundary. (c, f) 1% Nb-doped TiO_2(110) sample. (g) Representative PL decays for all samples. (h) PL lifetime distributions of undoped, 0.5% Nb and 1% Nb samples. (i) PL lifetime values averaged over a set of images for each sample.

d). Such values are seemingly smaller than the lifetimes obtained for rutile single crystals using time-resolved photoelectron spectroscopy; however, here we measured a signal averaged over hundreds of nm in the bulk, compared to the purely surface effect measured by Ozawa et al. [73]. We show that PL lifetimes can also be tuned by doping, where Nb substitution limits charge carrier dynamics, resulting in singular exponential behavior and a drop in PL lifetimes to 900 ps (for 0.5 wt% doping) and 430 ps (1 wt%). These values are in good agreement with previous studies on doped TiO_2 nanoparticles, in which 480 ps lifetimes were measured for an Nb concentration of 0.6 at.% (0.7 wt%) [61]. Surprisingly, the PL dynamics of the doped samples were insensitive in a reduced state (see Fig. 6 d - f), unlike the undoped rutile. Therefore, the origins of changes in PL dynamics via the self-doping of oxygen vacancies during reduction and substitutional aliovalent doping, respectively, differed.

As we assume that both undoped and doped rutile TiO_2 have similar PL emission spectra, as was already proven by Yamada et al. [4], differences must originate from the different density of defects and donated charge carriers. The influence of doping on the photocarrier dynamics is twofold. With more pentavalent niobium atoms present, the number of Ti^{3+} increases, and therefore more charge carriers could be trapped in these defect centers [23]. This could lead to the suppression of recombination and, consequently, to a PL lifetime increase. At the same time, the charge carrier density itself is enhanced as aliovalent Nb atoms donate electrons to the matrix, which then preferentially form polarons [74]. This would result in electron–electron-hole Auger processes becoming enhanced and a faster decay rate of photogenerated carriers, also contributing to the lower PL intensity. Moreover, other mechanisms, including the Shockley – Read – Hall recombination and self-trapped exciton (STE) processes, could play a role [75]. In order to resolve the impact of those main contributions (trapping and Auger processes) in more detail, we follow a simple rate equation describing the decay of charge carriers n [4]:

$$\frac{dn}{dt} = -An - Bn^2 - CN_e^2 n \quad (1)$$

where A is the monomolecular nonradiative recombination coefficient, representing single-carrier trapping processes, B is the bimolecular radiative recombination coefficient, C is the Auger recombination coefficient that involves three carriers, such as the electron–electron-hole and electron-hole-hole processes, n is the photogenerated carrier concentration, and N_e stands for excess electrons donated by doping. The measured PL intensity is therefore proportional to B $I_{PL} \propto Bn^2$.

The Auger component is approximated as being dependent on $N_e{}^2 n$ instead of n^3, as the concentration of photogenerated charge carriers n due to the two-photon absorption is much lower than the charge carriers donated by the Nb donors. It could be estimated as:

$$n = \frac{\beta F^2 t}{2\hbar\nu}$$

where β is a two-photon absorption coefficient that we assume, for the bulk rutile, is on the order of 0.9 mm/GW (for similar conditions of 1.58 eV (774 nm) photon energy and a 290 fs pulse laser) [76], F is a laser power density that was approximately 2 mW/μm^2, t is the time of interaction, here 0.3 ms (80 s for image / (512 × 512) pixels) and $h\nu$ the photon energy (2.7 × 10^{-19} J for 740 nm). This estimation results in a concentration of photogenerated electron-hole pairs of 10^{15} cm^{-3}, which is orders of magnitude smaller than the concentration of excess electrons in the Ti 3d band donated by either extrinsic Nb doping or the self-doping of oxygen vacancies upon reduction [47]. Therefore, as we are far from the saturation of absorption, we probe the pure changes in charge carrier dynamics due to the different defects' presence in rutile TiO_2, and laser beam-induced effects can also be neglected.

Our measurements entailed two-photon excitation and emission with a low quantum yield. Hence, the B coefficient could be neglected in Eq. (1) due to the low PL efficiency and PL lifetime being a simple function of donated d-type electrons:

$$\tau = (A + CN_e{}^2)^{-1}$$

For the two doping concentrations investigated, N_e would be equal to 1.3 × 10^{20} cm^{-3} (0.43 at.%) and 2.6 × 10^{20} cm^{-3} (0.86 at.%). For measured PL lifetimes of 883 ps (0.43%) and 417 ps (0.86%), these coefficients yield A = 3.57 × 10^8 s^{-1} and C = 1.25 × 10^{-32} cm^6 s^{-1}, which is in agreement with the values calculated by Yamada and Kanemitsu (A = 1.9 × 10^7 s^{-1} and C = 1.0 × 10^{-32} cm^6 s^{-1}) [4]. However, such a simplistic approach neglects the compensation mechanisms, which may significantly affect the donated electron concentration, i.e., there could be a compensation as high as 99.42%, reported for the 10% Nb occupation of Ti sites at 10^{-5} mbar O_2 and 50% compensation for 10^{-9} torr O_2 at 750 °C [77]. When also including the activation energy for electron transport in Nb-doped TiO_2 of approximately 80 meV, the ratio of localized polaronic to free electrons occupancy would be 1:20 at RT [78]. This would yield free carrier concentrations of 6.5 × 10^{18} cm^{-3} and 1.3 × 10^{19} cm^{-3} for 0.43% and 0.86% doping levels, respectively, where the rest electrons are dressed up in small and large polarons. Taking this correction into account, the final coefficients would be A = 2.11 × 10^8 s^{-1} and C = 5.0 × 10^{-30} cm^6 s^{-1}.

Nevertheless, this substantial content of the nonradiative Auger recombination coefficient is one reason for the observed PL lifetime suppression for increasing the doping of TiO_2. A similar observation was made for the case of Nb- and La-doped $SrTiO_3$ crystals where, in general, PL lifetimes drop with increasing concentrations of donated electrons [44,79].

In oxides, reduction results in the formation oxygen vacancies and the charge carrier concentrations increase. The density of oxygen vacancies V_O formed in Nb-doped TiO_2 during thermal annealing under heavily reducing conditions (1000 °C for 1 h) is on the order of 3 × 10^{19} cm^{-3}, as has already been measured via thermogravimetric analysis [3]. Here, the conditions were much less reducing (below 10^{-7} mbar of O_2) and the estimated V_O concentration was in the range of 1 × 10^{17} cm^{-3}. This is much below the concentration of excess electrons donated by extrinsic doping in the Nb-doped TiO_2 matrix, and therefore reduction does not change the carrier dynamics and hence PL lifetimes (compare Fig. 6i). Our PL lifetime data indicate, however, that oxygen vacancies formed in undoped TiO_2 via reduction according to our protocol, are playing a dominating role, as the lifetime of the slow PL decay component increases more than twice, to 4.6 ns (Fig. 6a and d). Therefore, the trapping near oxygen vacancy sites is the predominant process that enhances charge carriers' separation and, in turn, slows down their recombination. Similar behavior was observed in vacuum-annealed $SrTiO_3$ crystals in which positron lifetime observations indicate lifetime increases compared to untreated $SrTiO_3$ (121–151 ps to 260–276 ps), which was described as an influence of Sr and oxygen vacancy complexes [80].

To conclude the PL dynamic measurements, the PL lifetimes of all TiO_2 rutile samples with different doping levels and reduction states measured in this study are presented in Table 1. The values are averaged over a few large-scale images for each sample.

To demonstrate that we are dealing with a real two-photon process, the dependence of PL intensity and lifetimes on laser power was investigated, and the results are shown in Fig. 7. The power dependence on the observed PL intensity is purely quadratic and fits well with one parameter for both 0.5 wt% Nb-doped TiO_2 bulk and boundary as well as a rutile with a 1% Nb doping level (Fig. 7 a). The PL lifetime is also independent of the incident light power (Fig. 7 b), suggesting that we remain far from the saturation of absorption–emission processes. Additionally, no light irradiation-induced damage to the investigated crystals was observed when the same area was assessed using the increasing laser power and back to low power measurements. Fig. 7 c presents the PL lifetimes of a doped rutile TiO_2 following two-photon excitation with the light of wavelengths in the range between 720 nm (2 × 1.72 = 3.44 eV) and 860 nm (2 × 1.44 = 2.88 eV). No significant change in the charge carrier dynamics was observed for either doping level. This observation serves as proof that the excitation occurs in a defect state below the stoichiometric rutile conduction band, as the reported bandgap width is in the range of 3.1–3.3 eV. Therefore, the above-mentioned description of electron-hole pair creation is valid for a broader spectrum of the incident light, making the doped rutile a promising candidate for optoelectronic devices that operate in sunlight.

4. Conclusions

In summary, in this study we confirmed that PL in rutile TiO_2 is heavily dependent on the oxide defect state. The use of two-photon excitation, in combination with FLIM microscopy, enabled us to differentiate between effects related to intrinsic or extrinsic defects of a different dimensionality. Specifically, the photoluminescence dynamics in extended defects differed compared to the bulk TiO_2, as experimentally-observed ordered arrays of dislocations in an Nb-doped rutile bicrystal boundary contributes to lower PL intensities and shorter lifetimes. This situation can be reversed through the use of thermal reduction, which does not affect the bulk PL properties of Nb-doped TiO_2 but enhances the intensity and lifetimes at the boundary. We have also

Table 1
Averaged PL lifetimes for rutile TiO_2(1 1 0) single crystals with Nb doping levels from 0 to 1 wt% (for undoped samples, only the long decay was taken into account). The lifetimes are shown with statistical errors in picoseconds.

Sample	Photoluminescence lifetimes [ps]			
	Undoped TiO_2(1 1 0)	0.5% Nb TiO_2(1 1 0)		1% Nb TiO_2(1 1 0)
		Matrix	Boundary	
As received	2025 ± 31	862.9 ± 8.9	782 ± 15	417 ± 16
Reduced	4630 ± 116	885 ± 11	986 ± 21	448 ± 17
Oxidized	–	528.1 ± 8.2	519 ± 10	–

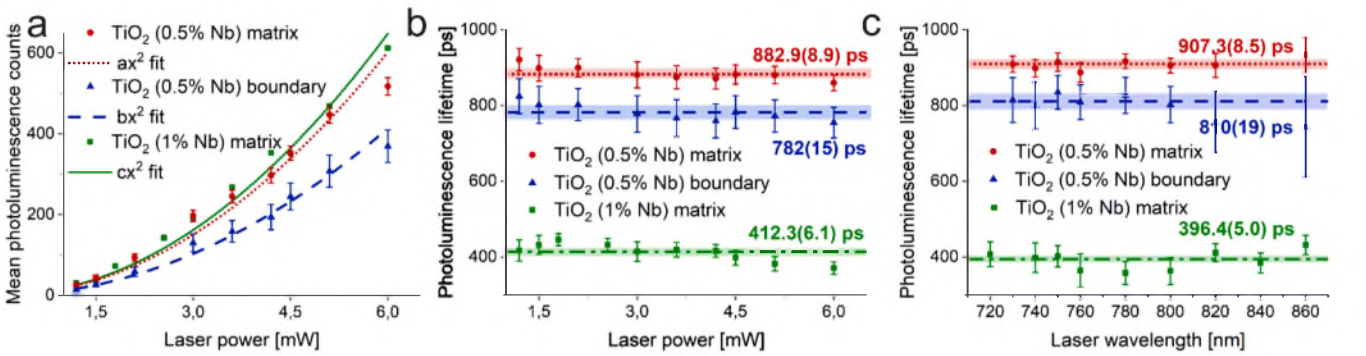

Fig. 7. Laser power and wavelength dependence on the PL lifetimes and intensities of the rutile TiO_2 with two donor doping levels. (a) Intensity increases with laser power and exhibits a purely quadratic characteristic for the boundary and bulk of 0.5% and 1% Nb-doped TiO_2, whereas the PL lifetimes are constant, regardless of the laser power (b). (c) PL lifetimes are independent of the incident photon energy for the range of (720–860 nm) for both Nb concentrations.

studied the influence on the PL dynamics of one of the most common donor doping. The increase in pentavalent Nb doping in the rutile crystal enhances the non-radiative Auger processes, resulting in a drop in the PL lifetimes from 2 ns for the undoped, through 900 ps for 0.5 wt% content, to 433 ps for a 1% Nb concentration. Therefore reduction finally leads to the longer PL lifetimes in the undoped rutile TiO_2, whereas shorter PL is observed for the Nb doping. Interestingly, PL lifetimes proved to be independent of the energy of the incident photon pair (in the range of 2.88–3.44 eV), which proves that absorption is realized to the bandgap Ti 3d state.

The suppression of nonradiative recombination is critical for achieving high levels of efficiency in optoelectronic devices. Our results suggest that reduction may pave the way to enhancing the photocatalytic behavior of real titanium oxide materials, such as thin films with the high densities of grain boundaries, via increasing the photogenerated charge carriers' lifetimes.

CRediT authorship contribution statement

Dominik Wrana: Conceptualization, Investigation, Methodology, Visualization, Writing – original draft. **Thomas Gensch:** Investigation, Methodology, Data curation. **Benedykt R. Jany:** Investigation, Data curation, Formal analysis. **Karol Cieslik:** Writing – review & editing. **Christian Rodenbücher:** Conceptualization, Writing – review & editing. **Grzegorz Cempura:** Investigation, Data curation. **Adam Kruk:** Resources. **Franciszek Krok:** Supervision, Funding acquisition.

Declaration of Competing Interest

The authors declare that they have no known competing financial interests or personal relationships that could have appeared to influence the work reported in this paper.

Acknowledgements

We gratefully acknowledge Prof. Kristof Szot for fruitful discussions and help with the with interpreting the data. Support from the Polish National Science Center (UMO-2018/29/B/ST5/01406) and the SciMat Priority Research Area budget under the Strategic Programme Excellence Initiative at the Jagiellonian University is also acknowledged.

Appendix A. Supplementary material

Supplementary data to this article can be found online at https://doi.org/10.1016/j.apsusc.2021.150909.

References

[1] W.-J. Yin, B.o. Wen, C. Zhou, A. Selloni, L.-M. Liu, Excess electrons in reduced rutile and anatase TiO2, Surf. Sci. Rep. 73 (2) (2018) 58–82, https://doi.org/10.1016/j.surfrep.2018.02.003.
[2] P. Ren, M. Song, J. Lee, J. Zheng, Z. Lu, M. Engelhard, X. Yang, X. Li, D. Kisailus, D. Li, Edge Dislocations Induce Improved Photocatalytic Efficiency of Colored TiO2, Adv. Mater. Interfaces 6 (17) (2019) 1901121, https://doi.org/10.1002/admi.201901121.
[3] D. Wrana, C. Rodenbücher, M. Krawiec, B.R. Jany, J. Rysz, M. Ermrich, K. Szot, F. Krok, Tuning the surface structure and conductivity of niobium-doped rutile TiO<inf>2</inf>single crystals via thermal reduction, PCCP 19 (2017), https://doi.org/10.1039/c7cp03136j.
[4] Y. Yamada, Y. Kanemitsu, Blue photoluminescence of highly photoexcited rutile TiO2: Nearly degenerate conduction-band effects, Phys. Rev. B - Condensed Matter & Mater. Phys. 82 (2010) 113103, https://doi.org/10.1103/PhysRevB.82.113103.
[5] Y. Yamada, Y. Kanemitsu, Photoluminescence spectrum and dynamics in highly photoexcited rutile TiO2, Phys. Status Solidi (c) 8 (2011) 104–107, https://doi.org/10.1002/pssc.201000642.
[6] R.A.C. Amoresi, V. Teodoro, G.F. Teixeira, M.S. Li, A.Z. Simões, L.A. Perazolli, E. Longo, M.A. Zaghete, Electrosteric colloidal stabilization for obtaining SrTiO3/TiO2 heterojunction: Microstructural evolution in the interface and photonics properties, J. Eur. Ceram. Soc. 38 (4) (2018) 1621–1631, https://doi.org/10.1016/j.jeurceramsoc.2017.10.056.
[7] H. Matsuzaki, Y. Matsui, R. Uchida, H. Yada, T. Terashige, B.-S. Li, A. Sawa, M. Kawasaki, Y. Tokura, H. Okamoto, Photocarrier dynamics in anatase TiO2 investigated by pump-probe absorption spectroscopy, J. Appl. Phys. 115 (5) (2014) 053514, https://doi.org/10.1063/1.4864219.
[8] B. Du, Q.i. Wei, Y. Cai, T. Liu, B.o. Wu, Y. Li, Y. Chen, Y. Xia, G. Xing, W. Huang, Crystal face dependent charge carrier extraction in TiO2/perovskite heterojunctions, Nano Energy 67 (2020) 104227, https://doi.org/10.1016/j.nanoen.2019.104227.
[9] F.M. Pesci, G. Wang, D.R. Klug, Y. Li, A.J. Cowan, Efficient suppression of electron-hole recombination in oxygen-deficient hydrogen-treated TiO2 nanowires for photoelectrochemical water splitting, J. Phys. Chem. C 117 (48) (2013) 25837–25844, https://doi.org/10.1021/jp4099914.
[10] T. Bak, D. Chu, A.R. Francis, W. Li, J. Nowotny, Concentration of electrons at grain boundaries in TiO2 (rutile): Impact on charge transport and reactivity, Catal. Today 224 (2014) 200–208, https://doi.org/10.1016/j.cattod.2013.11.039.
[11] S. Chen, Y. Wang, J. Li, Z. Hu, H. Zhao, W. Xie, Z. Wei, Synthesis of black TiO2 with efficient visible-light photocatalytic activity by ultraviolet light irradiation and low temperature annealing, Mater. Res. Bull. 98 (2018) 280–287, https://doi.org/10.1016/j.materresbull.2017.10.036.
[12] T. Leshuk, R. Parviz, P. Everett, H. Krishnakumar, R.A. Varin, F. Gu, Photocatalytic activity of hydrogenated TiO2, ACS Appl. Mater. Interfaces 5 (6) (2013) 1892–1895, https://doi.org/10.1021/am302903n.
[13] R. Sun, Z. Wang, N. Shibata, Y. Ikuhara, A dislocation core in titanium dioxide and its electronic structure, RSC Adv. 5 (24) (2015) 18506–18510, https://doi.org/10.1039/C4RA15278F.
[14] E. Maras, M. Saito, K. Inoue, H. Jónsson, Y. Ikuhara, K.P. McKenna, Determination of the structure and properties of an edge dislocation in rutile TiO2, Acta Mater. 163 (2019) 199–207, https://doi.org/10.1016/j.actamat.2018.10.015.
[15] S.I. Cha, K.H. Hwang, Y.H. Kim, M.J. Yun, S.H. Seo, Y.J. Shin, J.H. Moon, D.Y. Lee, Crystal splitting and enhanced photocatalytic behavior of TiO2 rutile nano-belts induced by dislocations, Nanoscale 5 (2) (2013) 753–758, https://doi.org/10.1039/C2NR33028H.
[16] X. Lü, X. Mou, J. Wu, D. Zhang, L. Zhang, F. Huang, F. Xu, S. Huang, Improved-Performance Dye-Sensitized Solar Cells Using Nb-Doped TiO_2 Electrodes: Efficient Electron Injection and Transfer, Adv. Funct. Mater. 20 (3) (2010) 509–515, https://doi.org/10.1002/adfm.200901292.
[17] G. Liu, W. Li, R. Bi, C. Atangana Etogo, X.-Y. Yu, L. Zhang, Cation-Assisted Formation of Porous TiO2-x Nanoboxes with High Grain Boundary Density as

Efficient Electrocatalysts for Lithium-Oxygen Batteries, ACS Catal. 8 (3) (2018) 1720–1727, https://doi.org/10.1021/acscatal.7b04182.
[18] L. Porz, T. Frömling, A. Nakamura, N. Li, R. Maruyama, K. Matsunaga, P. Gao, H. Simons, C. Dietz, M. Rohnke, J. Janek, J. Rödel, Conceptual Framework for Dislocation-Modified Conductivity in Oxide Ceramics Deconvoluting Mesoscopic Structure, Core, and Space Charge Exemplified for $SrTiO_3$, ACS Nano 15 (6) (2021) 9355–9367, https://doi.org/10.1021/acsnano.0c0449110.1021/acsnano.0c04491.s001.
[19] S. Wu, M.Y. Manuputty, Y. Sheng, H. Wang, Y. Yan, M. Kraft, R. Xu, Flame Synthesized Blue TiO 2–x with Tunable Oxygen Vacancies from Surface to Grain Boundary to Bulk, Small, Methods 5 (2) (2021) 2000928, https://doi.org/10.1002/smtd.v5.210.1002/smtd.202000928.
[20] S.-Y. Choi, J.P. Buban, M. Nishi, H. Kageyama, N. Shibata, T. Yamamoto, S.-J.-L. Kang, Y. Ikuhara, Dislocation structures of low-angle boundaries in Nb-doped SrTiO 3 bicrystals, in, J. Mater. Sci. 41 (9) (2006) 2621–2625, https://doi.org/10.1007/s10853-006-7824-9.
[21] H. Du, C.-L. Jia, L. Houben, V. Metlenko, R.A. De Souza, R. Waser, J. Mayer, Atomic structure and chemistry of dislocation cores at low-angle tilt grain boundary in SrTiO3 bicrystals, Acta Mater. 89 (2015) 344–351.
[22] P. Gao, S. Yang, R. Ishikawa, N. Li, B. Feng, A. Kumamoto, N. Shibata, P. Yu, Y. Ikuhara, Atomic-Scale Measurement of Flexoelectric Polarization at SrTiO3 Dislocations, Phys. Rev. Lett. 120 (2018), https://doi.org/10.1103/PhysRevLett.120.267601.
[23] D. Marrocchelli, L. Sun, B. Yildiz, Dislocations in SrTiO3: easy to reduce but not so fast for oxygen transport, J. Am. Chem. Soc. 137 (2015) 4735–4748.
[24] L. Sun, D. Marrocchelli, B. Yildiz, Edge dislocation slows down oxide ion diffusion in doped CeO2 by segregation of charged defects, Nat. Commun. 6 (1) (2015), https://doi.org/10.1038/ncomms7294.
[25] K. Szot, C. Rodenbücher, G. Bihlmayer, W. Speier, R. Ishikawa, N. Shibata, Y. Ikuhara, Influence of dislocations in transition metal oxides on selected physical and chemical properties, Crystals 8 (6) (2018) 241, https://doi.org/10.3390/cryst8060241.
[26] C. Rodenbücher, D. Wrana, T. Gensch, F. Krok, C. Korte, K. Szot, The electronic properties of extended defects in srtio3—a case study of a real bicrystal boundary, Crystals 10 (2020) 1–19, https://doi.org/10.3390/cryst10080665.
[27] P. Wang, W. Yi, J. Chen, S. Ito, C. Cui, T. Sekiguchi, Oxygen vacancy migration along dislocations in SrTiO3 studied by cathodoluminescence, J. Phys. D Appl. Phys. 52 (47) (2019) 475103, https://doi.org/10.1088/1361-6463/ab3b3e.
[28] W. Lin, D. Li, Y. Su, H. Shi, L.i. Wang, X. Cao, Y. Meng, H. Zhao, Nondestructive Visualization of Interfacial Conducting Inhomogeneities in Memristive Oxides by Electroluminescence, Adv. Mater. Interfaces 8 (1) (2021) 2001617, https://doi.org/10.1002/admi.v8.110.1002/admi.202001617.
[29] W. Yi, J. Chen, T. Sekiguchi, Electron-beam-induced current and cathodoluminescence study of dislocations in SrTiO3, Crystals 10 (2020) 1–8, https://doi.org/10.3390/cryst10090736.
[30] D.K. Pallotti, L. Passoni, P. Maddalena, F. Di Fonzo, S. Lettieri, Photoluminescence Mechanisms in Anatase and Rutile TiO2, J. Phys. Chem. C 121 (16) (2017) 9011–9021, https://doi.org/10.1021/acs.jpcc.7b0032110.1021/acs.jpcc.7b00321.s001.
[31] K. Fujihara, S. Izumi, T. Ohno, M. Matsumura, Time-resolved photoluminescence of particulate TiO2 photocatalysts suspended in aqueous solutions, J. Photochem. Photobiol.: A Chem. 132 (1-2) (2000) 99–104, https://doi.org/10.1016/S1010-6030(00)00204-5.
[32] J. Tong, Z. Song, D.H. Kim, X. Chen, C. Chen, A.F. Palmstrom, P.F. Ndione, M. O. Reese, S.P. Dunfield, O.G. Reid, J. Liu, F. Zhang, S.P. Harvey, Z. Li, S. T. Christensen, G. Teeter, D. Zhao, M.M. Al-Jassim, M.F.A.M. Van Hest, M.C. Beard, S.E. Shaheen, J.J. Berry, Y. Yan, K. Zhu, Carrier lifetimes of >1 ms in Sn-Pb perovskites enable efficient all-perovskite tandem solar cells, Science 364 (2019) 475–479, https://doi.org/10.1126/science.aav7911.
[33] K. Suhling, L.M. Hirvonen, J.A. Levitt, P.H. Chung, C. Tregidgo, A. Le Marois, D. A. Rusakov, K. Zheng, S. Ameer-Beg, S. Poland, S. Coelho, R. Henderson, N. Krstajic, Fluorescence lifetime imaging (FLIM): Basic concepts and some recent developments, Med. Photo. 27 (2015) 3–40, https://doi.org/10.1016/j.medpho.2014.12.001.
[34] W. Becker, ed., Advanced Time-Correlated Single Photon Counting Applications, Springer International Publishing, Cham, 2015. https://doi.org/10.1007/978-3-319-14929-5.
[35] D. Kuciauskas, D. Lu, S. Grover, G. Xiong, M. Gloeckler, Separating grain-boundary and bulk recombination with time-resolved photoluminescence microscopy, Appl. Phys. Lett. 111 (23) (2017) 233902, https://doi.org/10.1063/1.5010931.
[36] D. Comelli, A. Artesani, A. Nevin, S. Mosca, V. Gonzalez, M. Eveno, G. Valentini, Time-resolved photoluminescence microscopy for the analysis of semiconductor-based paint layers, Materials 10 (11) (2017) 1335, https://doi.org/10.3390/ma10111335.
[37] M. Ghirardello, S. Mosca, J. Marti-Rujas, L. Nardo, A. Burnstock, A. Nevin, M. Bondani, L. Toniolo, G. Valentini, D. Comelli, Time-Resolved Photoluminescence Microscopy Combined with X-ray Analyses and Raman Spectroscopy Sheds Light on the Imperfect Synthesis of Historical Cadmium Pigments, Anal. Chem. 90 (18) (2018) 10771–10779, https://doi.org/10.1021/acs.analchem.8b0166610.1021/acs.analchem.8b01666.s001.
[38] A. Artesani, M. Ghirardello, S. Mosca, A. Nevin, G. Valentini, D. Comelli, Combined photoluminescence and Raman microscopy for the identification of modern pigments: explanatory examples on cross-sections from Russian avant-garde paintings, Heritage Sci. 7 (2019) 17, https://doi.org/10.1186/s40494-019-0258-x.
[39] B. van Driel, A. Artesani, K.J. van den Berg, J. Dik, S. Mosca, B. Rossenaar, J. Hoekstra, A. Davies, A. Nevin, G. Valentini, D. Comelli, New insights into the complex photoluminescence behaviour of titanium white pigments, Dyes Pigm. 155 (2018) 14–22, https://doi.org/10.1016/j.dyepig.2018.03.012.
[40] A.S. Kristoffersen, S.R. Erga, B. Hamre, Ø. Frette, Testing fluorescence lifetime standards using two-photon excitation and time-domain instrumentation: Rhodamine B, coumarin 6 and lucifer yellow, J. Fluorescence 24 (4) (2014) 1015–1024, https://doi.org/10.1007/s10895-014-1368-1.
[41] M.J. Hÿtch, E. Snoeck, R. Kilaas, Quantitative measurement of displacement and strain fields from HREM micrographs, Ultramicroscopy 74 (3) (1998) 131–146, https://doi.org/10.1016/S0304-3991(98)00035-7.
[42] J.J.P. Peters, R. Beanland, M. Alexe, J.W. Cockburn, D.G. Revin, S.Y. Zhang, A. M. Sanchez, Artefacts in geometric phase analysis of compound materials, Ultramicroscopy 157 (2015) 91–97, https://doi.org/10.1016/j.ultramic.2015.05.020.
[43] T. Ohno, S. Ii, N. Shibata, K. Matsunaga, Y. Ikuhara, T. Yamamoto, High Resolution Microscopy Study for [001] Symmetric Tilt Boundary with a Tilt Angle of 66 in Rutile-type TiO 2 Bicrystal, n.d.
[44] C. Rodenbücher, T. Gensch, W. Speier, U. Breuer, M. Pilch, H. Hardtdegen, M. Mikulics, E. Zych, R. Waser, K. Szot, Inhomogeneity of donor doping in SrTiO3 substrates studied by fluorescence-lifetime imaging microscopy, Appl. Phys. Lett. 103 (16) (2013) 162904, https://doi.org/10.1063/1.4825367.
[45] J.K. Yan, K.Y. Kang, G.Y. Gan, Grain boundary segregation and the formation mechanism of secondary-phase in (Ce, Nb)-codoped TiO2 ceramics, Mater. Des. 99 (2016) 155–162, https://doi.org/10.1016/j.matdes.2016.03.031.
[46] M. Kamei, Localization of the photocatalytic reaction on the grain boundary of bicrystalline TiO2, Appl. Phys Express 1 (2008) 1012011–1012013, https://doi.org/10.1143/APEX.1.101201.
[47] K. Szot, M. Rogala, W. Speier, Z. Klusek, A. Besmehn, R. Waser, TiO_2—a prototypical memristive material, Nanotechnology. 22 (25) (2011) 254001, https://doi.org/10.1088/0957-4484/22/25/254001.
[48] M. Rogala, G. Bihlmayer, W. Speier, Z. Klusek, C. Rodenbücher, K. Szot, Resistive Switching of a Quasi-Homogeneous Distribution of Filaments Generated at Heat-Treated TiO_2 (110)-Surfaces, Adv. Funct. Mater. 25 (40) (2015) 6382–6389, https://doi.org/10.1002/adfm.v25.4010.1002/adfm.201500855.
[49] Q.K. Muhammad, L. Porz, A. Nakamura, K. Matsunaga, M. Rohnke, J. Janek, J. Rödel, T. Frömling, Donor and acceptor-like self-doping by mechanically induced dislocations in bulk TiO2, Nano Energy 85 (2021) 105944, https://doi.org/10.1016/j.nanoen.2021.105944.
[50] L. Zhang, W. Yu, C. Han, J. Guo, Q. Zhang, H. Xie, Q. Shao, Z. Sun, Z. Guo, Large Scaled Synthesis of Heterostructured Electrospun TiO 2 /SnO 2 Nanofibers with an Enhanced Photocatalytic Activity, J. Electrochem. Soc. 164 (9) (2017) H651–H656, https://doi.org/10.1149/2.1531709jes.
[51] K.V. Baiju, A. Zachariah, S. Shukla, S. Biju, M.L. P. Reddy, K.G.K. Warrier, Correlating photoluminescence and photocatalytic activity of mixed-phase nanocrystalline titania, Catal. Lett. 130 (1-2) (2009) 130–136, https://doi.org/10.1007/s10562-008-9798-5.
[52] G.W.P. Adhyaksa, S. Brittman, H. Āboliņš, A. Lof, X. Li, J.D. Keelor, Y. Luo, T. Duevski, R.M.A. Heeren, S.R. Ellis, D.P. Fenning, E.C. Garnett, Understanding Detrimental and Beneficial Grain Boundary Effects in Halide Perovskites, Adv. Mater. 30 (52) (2018) 1804792, https://doi.org/10.1002/adma.v30.5210.1002/adma.201804792.
[53] X. Wang, Z. Feng, J. Shi, G. Jia, S. Shen, J. Zhou, C. Li, Trap states and carrier dynamics of TiO2 studied by photoluminescence spectroscopy under weak excitation condition, PCCP 12 (2010) 7083–7090, https://doi.org/10.1039/b925277k.
[54] B. Choudhury, A. Choudhury, Tailoring luminescence properties of TiO2 nanoparticles by Mn doping, J. Lumin. 136 (2013) 339–346, https://doi.org/10.1016/j.jlumin.2012.12.011.
[55] R. Brüninghoff, K. Wenderich, J.P. Korterik, B.T. Mei, G. Mul, A. Huijser, Time-Dependent Photoluminescence of Nanostructured Anatase TiO2 and the Role of Bulk and Surface Processes, J. Phys. Chem. C 123 (43) (2019) 26653–26661, https://doi.org/10.1021/acs.jpcc.9b0689010.1021/acs.jpcc.9b06890.s001.
[56] V. Metlenko, A.H.H. Ramadan, F. Gunkel, H. Du, H. Schraknepper, S. Hoffmann-Eifert, R. Dittmann, R. Waser, R.A. De Souza, Do dislocations act as atomic autobahns for oxygen in the perovskite oxide SrTiO3? Nanoscale 6 (21) (2014) 12864–12876, https://doi.org/10.1039/C4NR04083J.
[57] K.K. Adepalli, J. Yang, J. Maier, H.L. Tuller, B. Yildiz, Tunable Oxygen Diffusion and Electronic Conduction in SrTiO3 by Dislocation-Induced Space Charge Fields, Adv. Funct. Mater. 27 (22) (2017) 1700243, https://doi.org/10.1002/adfm.v27.2210.1002/adfm.201700243.
[58] K.K. Adepalli, M. Kelsch, R. Merkle, J. Maier, Influence of line defects on the electrical properties of single crystal TiO2, Adv. Funct. Mater. 23 (14) (2013) 1798–1806, https://doi.org/10.1002/adfm.v23.1410.1002/adfm.201202256.
[59] H.-Y. Lee, J. Robertson, Doping and compensation in Nb-doped anatase and rutile TiO2, J. Appl. Phys. 113 (21) (2013) 213706, https://doi.org/10.1063/1.4808475.
[60] K. Yang, Y. Dai, B. Huang, Y.P. Feng, First-principles GGA+U study of the different conducting properties in pentavalent-ion-doped anatase and rutile TiO2, J. Phys. D Appl. Phys. 47 (2014), https://doi.org/10.1088/0022-3727/47/27/275101.
[61] S.G. Ghugal, S.S. Umare, R. Sasikala, Enhanced photocatalytic activity of TiO2 assisted by Nb, N and S multidopants, Mater. Res. Bull. 61 (2015) 298–305, https://doi.org/10.1016/j.materresbull.2014.10.006.
[62] M. Gallart, T. Cottineau, B. Hönerlage, V. Keller, N. Keller, P. Gilliot, Temperature dependent photoluminescence of anatase and rutile TiO2 single crystals: Polaron and self-trapped exciton formation, J. Appl. Phys. 124 (13) (2018) 133104, https://doi.org/10.1063/1.5043144.
[63] Z. Wang, M. Saito, K.P. McKenna, L. Gu, S. Tsukimoto, A.L. Shluger, Y. Ikuhara, Atom-resolved imaging of ordered defect superstructures at individual grain

boundaries, Nature 479 (7373) (2011) 380–383, https://doi.org/10.1038/nature10593.
[64] H.C. Sio, T. Trupke, D. Macdonald, Quantifying carrier recombination at grain boundaries in multicrystalline silicon wafers through photoluminescence imaging, J. Appl. Phys. 116 (24) (2014) 244905, https://doi.org/10.1063/1.4904963.
[65] M. Rogala, G. Bihlmayer, P. Dabrowski, C. Rodenbücher, D. Wrana, F. Krok, Z. Klusek, K. Szot, Self-reduction of the native TiO2 (110) surface during cooling after thermal annealing – in-operando investigations, Sci. Rep. 9 (1) (2019), https://doi.org/10.1038/s41598-019-48837-3.
[66] A.J. Atanacio, T. Bak, J. Nowotny, Niobium Segregation in Niobium Doped Titanium Dioxide (Rutile), J. Phys. Chem. C 118 (21) (2014) 11174–11185, https://doi.org/10.1021/jp4110536.
[67] D. Marrocchelli, L. Sun, B. Yildiz, Dislocations in SrTiO3: Easy to Reduce but Not so Fast for Oxygen Transport, J. Am. Chem. Soc. 137 (14) (2015) 4735–4748, https://doi.org/10.1021/ja513176u.
[68] C. Rodenbücher, K. Bittkau, G. Bihlmayer, D. Wrana, T. Gensch, C. Korte, F. Krok, K. Szot, Mapping the conducting channels formed along extended defects in SrTiO<inf>3</inf> by means of scanning near-field optical microscopy, Sci. Rep. 10 (2020), https://doi.org/10.1038/s41598-020-74645-1.
[69] J. Kwon, A.A. Sharma, J.A. Bain, Y.N. Picard, M. Skowronski, Oxygen vacancy creation, drift, and aggregation in TiO2-based resistive switches at low temperature and voltage, Adv. Funct. Mater. 25 (19) (2015) 2876–2883, https://doi.org/10.1002/adfm.201500444.
[70] H. Luitel, A. Sarkar, M. Chakrabarti, S. Chattopadhyay, K. Asokan, D. Sanyal, Positron annihilation lifetime characterization of oxygen ion irradiated rutile TiO2, Nuclear Instruments and Methods in Physics Research, Section B: Beam Interactions with Materials and Atoms. 379 (2016) 215–218. https://doi.org/10.1016/j.nimb.2016.04.014.
[71] W.R. Zipfel, R.M. Williams, W.W. Webb, Nonlinear magic: multiphoton microscopy in the biosciences, Focus On Opt. Imaging Nat. Biotechnol. 21 (11) (2003) 1369–1377, https://doi.org/10.1038/nbt899.
[72] P.B. Nair, V.B. Justinvictor, G.P. Daniel, K. Joy, V. Ramakrishnan, D.D. Kumar, P. V. Thomas, Structural, optical, photoluminescence and photocatalytic investigations on Fe doped Tio2 thin films, Thin Solid Films 550 (2014) 121–127, https://doi.org/10.1016/j.tsf.2013.10.112.
[73] K. Ozawa, M. Emori, S. Yamamoto, R. Yukawa, S. Yamamoto, R. Hobara, K. Fujikawa, H. Sakama, I. Matsuda, Electron-hole recombination time at TiO2 single-crystal surfaces: Influence of surface band bending, J. Phys. Chem. Lett. 5 (11) (2014) 1953–1957, https://doi.org/10.1021/jz500770c.
[74] A. Janotti, C. Franchini, J.B. Varley, G. Kresse, C.G. Van de Walle, Dual behavior of excess electrons in rutile TiO2, Physica Status Solidi - Rapid Res. Lett. 7 (3) (2013) 199–203, https://doi.org/10.1002/pssr.201206464.
[75] T.R. Senty, S.K. Cushing, C. Wang, C. Matranga, A.D. Bristow, Inverting transient absorption data to determine transfer rates in quantum dot-TiO2 heterostructures, J. Phys. Chem. C 119 (11) (2015) 6337–6343, https://doi.org/10.1021/jp512500g.
[76] C.C. Evans, J.D.B. Bradley, E.A. Martí-Panameño, Eric Mazur, Mixed two- and three-photon absorption in bulk rutile (TiO_2) around 800 nm, Opt. Express 20 (3) (2012) 3118, https://doi.org/10.1364/OE.20.003118.
[77] D. Morris, Y. Dou, J. Rebane, C. Mitchell, R. Egdell, D. Law, a. Vittadini, M. Casarin, Photoemission and STM study of the electronic structure of Nb-doped TiO2, Phys. Rev. B 61 (2000) 13445–13457, https://doi.org/10.1103/PhysRevB.61.13445.
[78] S.X. Zhang, D.C. Kundaliya, W. Yu, S. Dhar, S.Y. Young, L.G. Salamanca-Riba, S. B. Ogale, R.D. Vispute, T. Venkatesan, Niobium doped TiO2: Intrinsic transparent metallic anatase versus highly resistive rutile phase, J. Appl. Phys. 102 (1) (2007) 013701, https://doi.org/10.1063/1.2750407.
[79] H. Yasuda, Y. Kanemitsu, Dynamics of nonlinear blue photoluminescence and Auger recombination in SrTiO3, Phys. Rev. B - Condensed Matter & Mater. Phys. 77 (2008) 193202, https://doi.org/10.1103/PhysRevB.77.193202.
[80] R.A. Mackie, S. Singh, J. Laverock, S.B. Dugdale, D.J. Keeble, Vacancy defect positron lifetimes in strontium titanate, Physical Review B - Condensed Matter and Materials, Physics 79 (2009) 014102, https://doi.org/10.1103/PhysRevB.79.014102.